

Chapter 1

Introduction

Nanoparticles are defined as particles of less than 100 nm in diameter that exhibit new or enhanced size-dependent properties compared to larger particles of the same material ¹. Such changes arise due to three main reasons: i) an increase in the surface to volume ratio, ii) a change in the morphology of the crystal, and/or iii) quantum confinement effects^{2,3}. Quantum effects occur when the de Broglie wavelength associated with the free charge carriers becomes greater than the particle dimensions ². These size dependent properties have potential applications in catalysis^{3,4}, electronics⁵, medicine⁶⁻⁸ etc. Hence, there has been a growing interest in manufacturing nanoparticles of different materials.

Nanoparticles can be produced via vapor or liquid phase synthesis methods. In vapor phase nanoparticle synthesis, monomers are formed by thermal evaporation or laser ablation and then nucleate and grow in vacuum to form nanoparticles. Vapor-phase synthesis methods can produce large quantities of nanoparticles, but agglomeration and non-uniformity in particle size and shape are typical problems, especially at the smaller end of the nanometer range (<10 nm) ⁹. These problems are now avoided by using liquid-phase synthesis routes, as various methods of this type yield well dispersed and relatively uniform sized nanoparticles. Designing continuous flow high yield synthesis processes to form monodisperse particles is a major challenge that needs to be addressed in order to pursue fundamental and applied studies on these materials. A good understanding of the nanoparticle formation kinetics is required to model and optimize continuous flow processes. Kinetics is also the missing link between batch protocols and continuous flow reactors.

Nanoparticles of different sizes and polydispersity produced by different methods have varied uses, so accurate characterization of particle size is also critical. The most common characterization technique is Transmission Electron Microscopy (TEM) ⁸⁻¹³ or Scanning Electron Microscopy (SEM)¹⁰, which directly provides

information on nanoparticles size and shape., but dimensions can also be obtained using tools such as atomic force microscope (AFM) ², X-ray scattering⁹, Dynamic light scattering(DLS) ¹³, and UV-Visible spectrophotometry⁹, etc.

The objectives of this project are, i) To develop and optimize protocols to get repeatable results using this new stop flow module, and ii) To understand the kinetics of nucleation and growth of gold nanoparticles, using the stop flow module ¹⁴⁻¹⁶.

The rest of the report is structured as follows. Chapter 2 provides an introduction to the phenomena of Surface Plasmon Resonance (SPR), principals of Stop Flow Module (SFM), nucleation and growth models. Chapter 3 reports on the kinetics (nucleation & growth) of gold nanoparticle formation. Chapter 4 briefly discusses the materials and methods used. Chapter 5 provides an analysis of the results obtained, and Chapter 6 summarizes the work done.

Chapter 2

Background

2.1 Nanoparticle formation mechanism

2.1.1 LaMer model

LaMer et al.²¹ proposed a model for particle formation by chemical precipitation route. They proposed a mechanism with 3 stages (Figure 2.1). Stage 1: The concentration of monomer increases with time due to reaction. Nucleation does not begin at saturation concentration itself due to the surface energy required for creating a new solid surface.

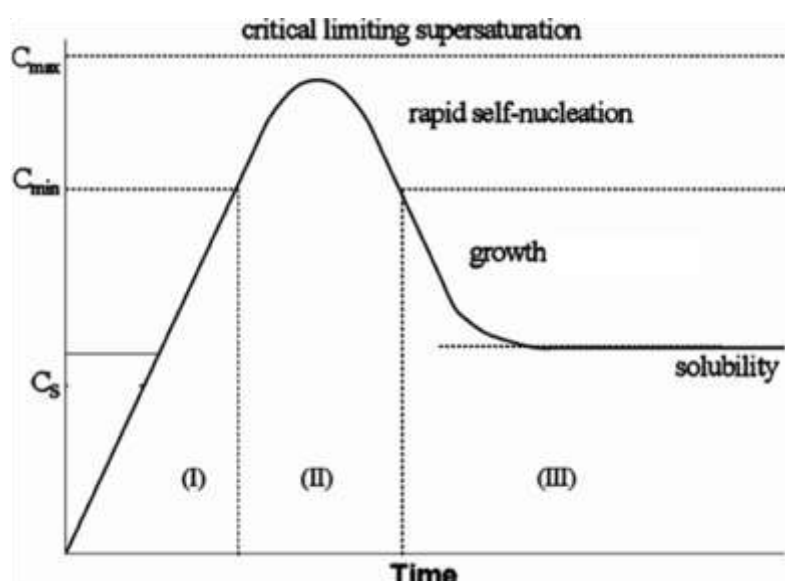


Figure 2.1: Schematic representation of concentration of dissolved sulfur molecules with respect to time in dilute sodiumthiosulphate and dilute hydrochloric acid system during nucleation and growth of sulfur monosols, proposed by LaMer.¹⁷

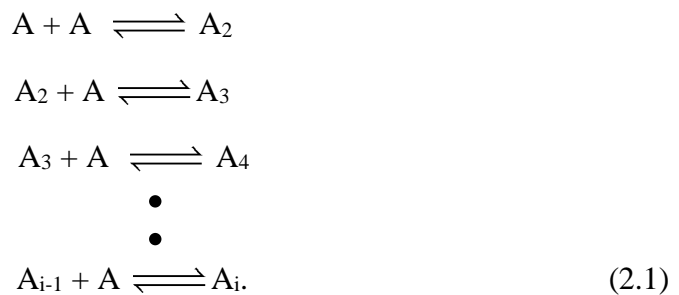
Stage 2: At this stage the system is very sensitive to concentration. The rate of nucleation tends to infinity for a small change in concentration. Rapid “self-nucleation” occurs and the rate of nucleation rapidly falls to zero (as concentration

drops due to rapid nucleation) and nucleation stops, Stage 3: The supersaturation is still present in the system, therefore the nuclei continue to grow monomer addition to surface of nuclei till the amount of monomer reaches a equilibrium due to balance of reaction and growth until all monomer is consumed. Hence, the final growth rate is controlled by reaction. For monodispersed particles to be formed, the nucleation time scale (phase II) must be very small compared to growth.

2.1.2 Nucleation mechanisms and induction time

There are two prevalent nucleation models. The classical nucleation theory proposed by Volmer, Becker, and Doring¹⁸, and the kinetic approach to nucleation proposed by Christiansen and Nielsen. The main difference between the two is that the former proposes a continuous dependence of nucleation rate (induction time) and critical nuclei size on the supersaturation, while the latter theory predicts a constant critical nuclei size over discrete range of supersaturation. The embryo's concentration is assumed to be in quasi-equilibrium in Becker-Doring theory, whereas the kinetic approach differs in assuming that the final rate determining step is in quasi-steady state, while all the previous steps are in quasi-equilibrium¹⁸.

According to the classical nucleation theory, clusters of particles (embryos) are formed due to statistical fluctuations by addition of one molecule (precursor) at a time¹⁹ as shown in equation 2.1. The distribution of the embryos is assumed to be in equilibrium. Once the critical size is crossed particles do not re-dissolve.



where, A represents monomers and A_i represents critical nuclei. Once the critical size is crossed, monomer addition is irreversible. The distribution of embryos is assumed

to be in equilibrium. Based on the above idea, Becker and Doring proposed the following expression for the rate of nucleation (\dot{N}_N).

$$\dot{N}_N = \dot{K} \exp(-\Delta G^* / k_B T) \quad (2.2)$$

where,

i is number of precursors or monomers present in critical nuclei,

\dot{K} is pre-exponential constant,

ΔG^* is the free energy change to transfer i particles from liquid phase to solid phase,

k_B is Boltzmann's constant,

T is temperature.

The change in free energy is obtained by adding the contribution due to free energy change per unit solid volume, and the free energy lost in creation of new surface. Classical nucleation theory assumes that density and interfacial energy of clusters is same as that of macroscopically large crystals. For any spherical cluster of size r , the free energy of formation is

$$\Delta G_j = -(4\pi/3)(r^3/v)kT \ln S + 4\pi r^2 \sigma \quad (2.3)$$

where,

S is supersaturation ratio, defined as ratio of concentration of precursor (C) to the equilibrium / saturation concentration of the precursor (C_o),

r is radius of cluster,

σ is interfacial energy/ unit area.

Critical nuclei size corresponding to the maximum of free energy is obtained as,

$$r_c = 2 \sigma v / kT \ln S \quad (2.4)$$

Correspondingly, the free energy barrier is given by

$$\Delta G^* = 16\pi\sigma^3 v^2 / 3(kT \{\ln S\})^2 \quad (2.5)$$

Therefore the rate at which critical nuclei are formed is given by,

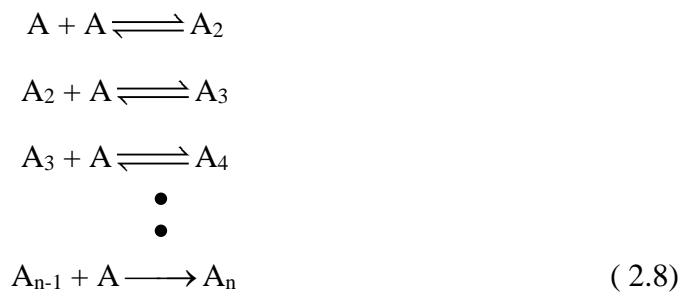
$$\dot{N}_N = k \exp(-16\pi\sigma^3 v^2 / 3 k^3 T^3 \{\ln S\})^2 \quad (2.6)$$

The induction time t_{ind} (an experimentally measurable quantity) is assumed to be inversely proportional to nucleation rate. It is the time required for the first particle(s) to be detected and includes the time required by a nanoparticle to nucleate (t_n) and grow (t_g) to a detectable size. Typically, $t_g \ll t_n$ and so $t_{ind} \sim t_n$.

$$t_{ind} \propto \exp(16\pi\sigma^3 v^2 / 3 k^3 T^3 \{\ln S\})^2 \quad (2.8)$$

Equation 2.7 implies a plot of t_{ind} vs $1/\{\ln S\}^2$ should be a straight line when temperature (T) is constant, according to classical nucleation theory¹⁹.

Becker and Doring assumed a quasi equilibrium distribution of embryo (cluster smaller than critical size) during nucleation, but they did not account for the time required to reach such a state. Also, classical nucleation theory assumes a continuous distribution of nuclei size, but for very small nuclei, the discrete atomic nature also needs to be considered. Christiansen and Nielsen proposed a mechanism that overcomes these limitations by assuming that the final critical nuclei forming step is irreversible and at quasi steady state.



The rate of formation of nuclei is then given by

$$d[A_n]/dt = rA^n = - (1/n)d[A]/dt \quad (2.9)$$

where, A is initial concentration of precursor, and A_n is concentration of critical nuclei and n is the order of equation, and r is a constant.

Induction time period (t_{ind}) is obtained by integrating equation 2.9 as

$$R = t_{ind} A^{(n-1)} \quad (2.10)$$

where, R is a constant.

2.1.3 Growth mechanisms

The process of additional material depositing on a particle is called growth¹⁰. When a colloidal particle is growing in conditions of supersaturation, the solute has to diffuse to the surface of colloidal particle and then has to be incorporated into the particle by surface reaction²⁰. The total flux of solute, J , passing through a spherical plane with radius x within the diffusion layer is given by Ficks law as,

$$J = 4\pi x^2 D \frac{dC}{dx} \quad \forall x \in (r, r + \delta) \quad (2.11)$$

where,

D = diffusivity

C = concentration of solute, r is particle radius, δ diffusion layer thickness. Then separating the variables C and r , and then integrating equation 2.11 (assuming J is constant in this range) gives

$$J = \frac{4\pi D r(r + \delta)}{\delta} (C_b - C_i) \quad (2.12)$$

where, C_b = concentration in bulk liquid, C_i = concentration of monomer at the surface of the particle. For surface reaction with a rate constant k (assuming simple first order reaction), rate of incorporation is given by

$$J = 4\pi r^2 k (C_i - C_e) \quad (2.13)$$

From mass balance,

$$dr/dt (= JV_m/4\pi r^2) \quad (2.14)$$

Eliminating C_i from equations 2.12, 2.13 and, then substituting for J from the equation 2.14, we get

$$\frac{dr}{dt} = \frac{\frac{D}{r} \left(1 + \frac{r}{\delta}\right) V_m (C_b - C_e)}{1 + \frac{D}{rk} \left(1 + \frac{r}{\delta}\right)} \quad (2.14)$$

where, V_m = molar volume of solid.

When in a diffusion controlled system ($\frac{D}{r} \ll k$) (Figure 2.2 a), equation 2.14 reduces to

$$\frac{dr}{dt} = \frac{D}{r} \left(1 + \frac{r}{\delta}\right) V_m (C_b - C_e) \quad (2.15)$$

For very small particles, $\frac{r}{\delta} \ll 1$. Therefore, equation 2.15 reduces to

$$\frac{dr}{dt} = \frac{D}{r} \left[V_m (C_b - C_e) \right] \quad (2.16)$$

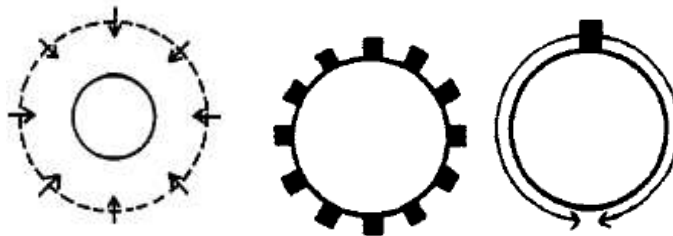


Figure 2.2: Schematic representation of different growth modes. a. Diffusion controlled growth, the arrows represent the diffusion of precursor from bulk across the diffusion boundary layer (dashed line). b. Polynuclear layer growth, the black protrusions represent all the nuclei deposited on growth surface c. Mononuclear layer growth²⁰, A single nuclei (black protrusion on particle surface) grows quickly on the old particle surface to form a new surface.

Hence for diffusion controlled growth, rate of change of size is inversely proportional to r (size of nanoparticles).

In reaction controlled reactions, if growth occurs by deposition of nuclei at many places on the surface, it is called polynuclear layer growth (Figure 2.2 b). If, growth occurs by deposition of single nucleus on the particle and then rapid two

dimensional growth of the nucleus on the particle surface, it is called mononuclear layer growth (Figure 2.2 c)²⁰. For polynuclear reaction controlled growth, rate of increase in size is independent of size.

This is obtained when $D \gg kr$ in equation 2.15.

$$dr/dt = k V_m (C_b - C_e) \quad (2.19)$$

In case of mononuclear layer growth, the rate of change of size is proportional to r^2 (surface)²⁰.

2.2 Surface Plasmon Resonance (SPR)

Gold colloids exhibit different colors depending on the size of the nanoparticle. This is due to a phenomenon called Surface Plasmon Resonance (SPR). SPR is the in-phase oscillation due to coherent excitation of all the 'free' electrons within the conduction band of metal nanoparticles by electric field component of electromagnetic waves (Figure 2.3).

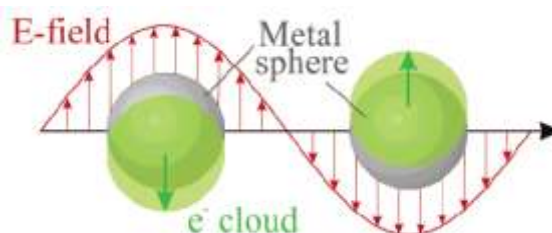


Figure 2.3: Schematic representation of surface plasmon resonance: Oscillation of electron cloud with respect to the metal sphere caused by the electric field component of incident light wave.²¹

In the case of nano-sized metals exhibiting surface plasmon absorption, optical spectrophotometry represents a viable approach for in-situ size monitoring²². In very small nanoparticles (< 2 nm), surface plasmon resonance (SPR) is strongly damped, and is absent. However, for noble metal nanoparticles of size > 2 nm, SPR occurs in the visible region. The surface plays a very important role in SPR as it alters the boundary conditions for polarizability of the metal and hence shifts the resonance band. Hence, SPR is a small particle effect and not a quantum size effect²³. One

useful feature of SPR is the dependence of the position and width on the particle size which can be computed using Mie's theory. Typically, for particle sizes $>20\text{nm}$, the SPR red shifts with increasing particle sizes¹⁰ and also broadens for larger particles due to increased radiation damping. Red shift is also observed for higher aspect ratio. Hence, it is possible to deduce the particle shape and size by observing resonance bands and linewidth²³. Mie explained the origin of surface Plasmon resonance in gold nanoparticles by solving Maxwell's equation for an electromagnetic wave interacting with small spheres. For nanoparticles less than 20 nm, only dipole oscillation of electron cloud contributes to excitation cross section. The extinction coefficient (σ_{ext}) is obtained as

$$\sigma_{\text{ext}}(\omega) = 9 \left(\frac{\omega}{c} \right) \epsilon_m^{3/2} V \frac{\epsilon_2(\omega)}{[\epsilon_1(\omega) + 2\epsilon_m]^2 + \epsilon_2(\omega)^2} \quad (2.20)$$

Where,

V is particle volume

ω is angular frequency of the exciting light

c is speed of light

ϵ_m , $\epsilon = \epsilon_1(\omega) + i\epsilon_2(\omega)$ are the dielectric functions of the surrounding medium and material itself, respectively.

Resonance condition is fulfilled when $\epsilon_1(\omega) = -2\epsilon_m$, if ϵ_2 is small or weakly dependent on ω . From the equation above we can see that λ_{max} of SPR band is independent of particle size (for $r < 20\text{ nm}$). This fact aids us to follow nanoparticle growth by monitoring absorbance at a single wavelength.

2.3 Stopped Flow Reactor (SFR)/ Stop Flow Module (SFM)

In precipitation reactions taking place in batch reactors, the supersaturation ratio will vary with position in the vessel as well as time. Since nucleation rate is a strongly non linear function of supersaturation, the measured nucleation rate varies widely. Hence, in order to study nucleation, we need well controlled hydrodynamic conditions. One way is to premix the reactants instantaneously to exclude variations in supersaturation²⁴. This helps to study fast growth kinetics as well.

There are two methods for studying the kinetics of a reaction, namely 1) steady state analysis, and 2) transient kinetics. Steady state analysis is laborious and tedious in nature, we change the conditions of the system and observe the transition from one equilibrium state to another with respect to time in transient state analysis. Slow reactions can be initiated by hand and studied but fast reactions need rapid-mixing equipment, to mix the reactants rapidly and to study the changes in the reaction mixture immediately. For fast reactions where optical signals are available, spectroscopic assays are useful. If optical signals are absent, the reaction is stopped after variable intervals of time by quenching the reaction mixture and is analyzed by other characterization techniques. But for rapid reactions there is a possibility of wrong results in quench flow mode, which arises due to improper quenching. Hence, in situ observations are preferred.

The stopped flow reactor gives reactant economy, and low dead time due to small volumes of reactants being handled efficiently in it. The Berger ball mixer and the stepping motors are the main components in SFM that make this feasible¹⁶.

The Berger ball mixer (Figure 2.4) is a four-jet ball mixer, which uses high velocities created in the wake behind the sphere to cause mixing. The spherical geometry creates a highly localized zone of intense turbulence with low pressure drop. It consists of two parts, the main body I, and the insert II. The solution A approaches the mixing chamber through four openings. Solution B approaches through a curved channel in the mixer holder. The solutions will meet at point 1 and travel around the hemisphere to point 2 and leave after mixing there²⁵. The time scale of mixing is of the order of milliseconds.

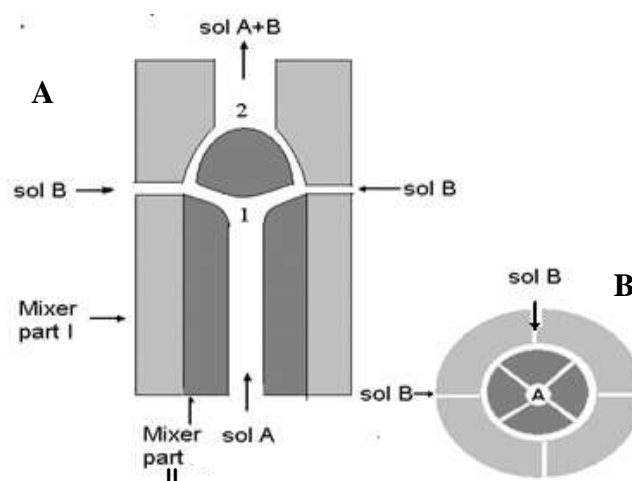


Figure 2.4: Schematic representation of the Berger ball mixer adapted from ref ³⁷. (a) Vertical section. (b) Horizontal section. The solution ‘A’ approaches the mixing chamber through four openings and Solution ‘B’ approaches through a curved channel in the mixer holder. The solutions will meet at point 1 and travel around the hemisphere to point 2.

The SFM basically consists of four syringes S1, S2, S3, and S4, each syringe driven by a stepping motor as shown in figure 2.5a. The mixer and flow lines are as shown in the schematic (Figure 2.5a). The mixture goes from the last mixer into the cuvette, where the reaction is followed ²⁵.

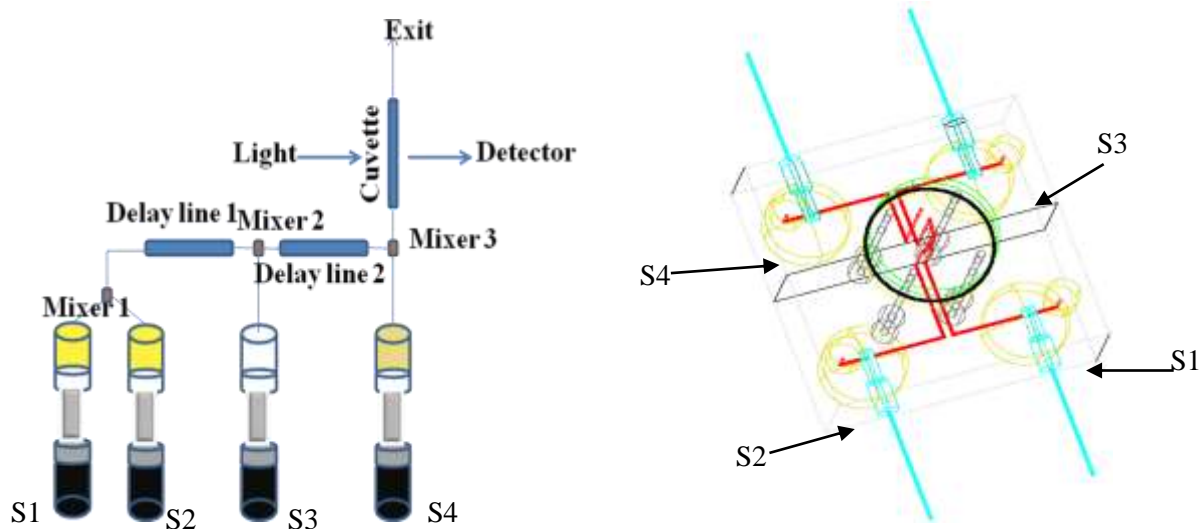


Figure 2.5: (a) Schematic representation of the SFM, showing the four syringes S1, S2, S3, and S4. The two mixers, the flow lines and the cuvette are also shown. (b) CAD drawing of the SFM flowlines, with the position of the four syringes marked by arrows [Acknowledgement: Mr. Prakash, Department of Chemical Engineering, IISc.]

The stop flow allows us to study the kinetics by following the absorbance at a particular wavelength with respect to time in the transient kinetics mode, the spectra could be tracked in spectral mode, and the time evolution of spectra (3D graph) could be followed in the Global mode, which pieces together kinetics obtained at different wavelengths.

Chapter 3

Literature Review

Metal nanoparticles can be produced by different methods. Many of the methods reported for the preparation of the nanoparticles are applicable to many metals across the periodic table ²⁶⁻²⁸. The material of current interest is gold. Gold nanoparticles of desired size and monodispersity can be prepared by the different protocols given in the literature ²⁹⁻³³. Different methods are used to characterize the nanoparticles produced, such as UV-Vis spectrophotometry, Dynamic light scattering, TEM ^{10, 13}, and AFM ³³.

3.1 Studies of nanoparticle nucleation

Very few reports in the literature, report on the nucleation/ induction times of nanoparticles. Turkevich reported on nucleation and growth of gold nanoparticles synthesized by reducing gold chloride with sodium citrate ¹⁰. In this section, we shall discuss his work on gold nanoparticle nucleation. Since, it was difficult to observe the nuclei directly, the nuclei were grown in separate growth solutions. Assuming that there was no fresh nucleation in the growth medium, and that the polynuclear surface reaction was controlling, the final size distribution curve and final particle size were used to determine nucleation rate and nuclei size¹⁰.

The nucleation rate curves so obtained showed presence of induction time. The general trend of the nucleation rate curves obtained were characteristic of autocatalytic reaction. On using acetone dicarboxylic acid directly as reducing agent, there was negligible induction time. This showed that acetone dicarboxylic acid was an intermediate that was involved in gold nanoparticle formation by citrate method and its formation involved autocatalytic process. They proposed “organizer mechanism” based on their observations. They proposed that acetone dicarboxylic acid was acting as an organizer that brings gold atoms together. They support this

with the known fact that acetone dicarboxylic acid is capable of forming complexes with metal ions.

Ghader et al.,³⁴ studied the induction time variation with supersaturation during the precipitation of silver nanoparticles formed by reducing silver nitrate with hydrazine. The interfacial tension was estimated using classical nucleation theory. Based on analysis using kinetic theory of nucleation, the order of nucleation was reported to be 0.24, which indicates that either heterogeneous nucleation was occurring or the redox reaction to form silver atoms was the rate limiting step.

Andresscu et al.³⁵, studied gold nanoparticle synthesis at room temperature by reduction of gold salt using iso-ascorbic acid. Induction period was observed in all their reactions. They attributed induction time to the time required for reduction of Au^{3+} to Au^+ resulting in linear AuCl_2^- complex ions that don't absorb in UV-Vis. They proposed that in the subsequent step, these Au(I) species are reduced to gold atoms, which undergo nucleation immediately after critical supersaturation is attained and form nanoparticles by rapid diffusional growth. An increase in the concentration of gold solution caused an acceleration of reduction reactions in the homogeneous phase. This was corroborated by the shortening of induction time that precedes the nucleation. Depending on the size of the resulting metal particle was found to be only slightly, depend on the concentration of gold salt solution.

3.2 Kinetic studies of nanoparticle growth

Kinetic studies of nanoparticle growth are basically of two types, in-situ methods and ex-situ methods. In-situ methods usually involve characterization using UV-Visible spectrophotometry^{20,36}, SAXS¹⁹ etc while the reaction is progressing. The ex-situ analysis is carried out by AFM³³, TEM^{10, 37}, SEM¹⁰ by sampling the reaction mixture at various intervals and determining particle size distribution.

3.2.1 Gold nanoparticle formation – Ex-situ studies

Studies on growth by gold nanoparticle formation by Turkevich revealed that gold nanoparticle growth with citrate or hydroxylamine hydrochloride as reducing agent was following exponential trend¹⁰. This was based on the observation that the ratio of the final particles produced was same as the ratio of the initial particle sizes (particles of two different sizes) introduced in the growth mixture. They could not explain the reason for the observed exponential growth rate.

Nanoparticle synthesis by Turkevich method was studied using ex-situ TEM analysis by Pong et al.³⁷ to understand the mechanism of nucleation and growth. Ex-situ TEM analysis of the process was done by quenching aliquot's from the reaction mixture by rapid cooling and sampling on carbon grids. During the synthesis, the color changes in the following order as the reaction proceeds: pale yellow, colorless, very dark blue, purple and finally ruby red. They observed nanoclusters of about 5 nm diameter self-assembled to form an extensive network of nanowires (intermediates). The diameter of the nanowires progressively increased in size, and at the same time the connected network is fragmented into small segments before the final spherical particles were formed. They put forward a modified nanocrystal growth mechanism, which doesn't follow LaMer model. They also proposed that a process similar to Ostwald's ripening might be taking place, to aid in fragmentation of spherical particles from chains³⁷.

Kimling et al.⁹ also studied the kinetics of gold nanoparticle formation by Turkevich method. UV-Vis spectrophotometry, X-ray scattering and electron microscopy were used to characterize the gold nanoparticles produced. Multiple steps of primary and secondary clustering were observed, which led to polycrystallites being formed. Larger particles were formed when citrate concentration was reduced. They concluded that stabilizing agent plays a dominating role compared to supersaturation and coarsening in determining the kinetics of nanoparticle formation.

3.4.2 Gold nanoparticle formation – In-situ studies

Gold nanoparticles prepared by alcoholic reduction of Au(III) ions in presence of a polymeric stabilizer was investigated using in-situ UV-Vis characterization by Salvati et al.³⁶⁻³⁸ They obtained UV-Vis spectra of the reacting mixture as a function of time at various temperatures. They used the Lorentzian method of deconvolution to estimate the contributions to UV-vis absorbance spectra from the following (i) Au³⁺ ions, (ii) 5d \rightarrow 6sp interband transition in solid atoms, and (iii) Surface Plasmon Resonance of nanoparticles. The radius was found to vary linearly with time for temperatures above 70°C. This indicates that the growth is surface reaction controlled.

Abecassis et al.²² studied the nucleation and growth of gold nanoparticle formation using the monophasic synthesis protocol proposed by Jana et al.³². The gold nanoparticles were obtained by reduction of borohydride salt (BH₄⁻) of a gold solubilised in toluene by a cationic surfactant (DDAB) in the presence of an excess of alkyl derivative ligands, either decylamine or decanoic acid. A rapid mixing stopped flow reactor [similar to the one used in this study] was used to conduct in-situ analysis of gold nanoparticles growth. UV-Visible spectrophotometry, Small angle X-ray scattering (SAXS) and Wide angle X-ray scattering (WAXS) were used to characterize the size of gold nanoparticles formed. They studied the nucleation and growth of gold nanoparticles formation with a time resolution of 3 ms in UV-Visible spectrophotometer. They studied the temporal evolution of the UV absorbance at 540 nm (SPR of gold nanoparticles) and 400 nm (gold (III)-DDAB ion pair's characteristic band). They proposed that the ligands affected the final size of the particle, because they affect the nucleation and growth of the particles²².

Herrera et al.¹³ studied the kinetics of synthesis and agglomeration of gold nanoparticles in reverse micelles. A stopped flow reactor was used to make in-situ time-correlated UV-Vis absorption measurements. The peak wavelength of the surface plasmon resonance band showed a red shift due to agglomeration of particles greater than 8 nm in diameter. This red shift is due to increase in particle size with time resulting in particles of 25-85 nm. Dynamic light scattering and theoretical

analysis of total interaction energy between pairs of particles as a function of particle size also showed evidence of cluster formation. The particles grow up to a size of 8-10 nm and start agglomerating showing an red shift in the spectrum.

It is seen from these studies that identification of nucleation kinetics is not straight forward for reaction precipitation routes. It is not easy to correlate the contributions from reaction time and nucleation time to the changes in measured induction times. However, growth kinetics are surface reaction controlled or monomer supply limited.

Chapter 4

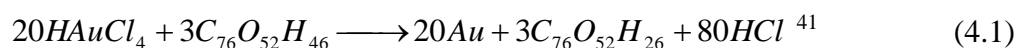
Materials and methods

4.1 Experimental set up

A rapid mixing, stopped flow reactor from Biologic Science Instruments (Cliax, France) is used to measure the time variation of absorbance. It consists of a stop flow module 400, an optical system MOS-200/M, and a microprocessor MPS-60. The specifications of SFM 400 include 4 syringes of 10 ml capacity each, one stepping motor per syringe, 1 to 3 mixers, and 25 to 1000 μ l ageing lines. The optical system has the following components and specifications: 150 W Xe or Xe(Hg) lamp, monochromator, wavelength range 180 to 999 nm (with Xe lamp it is only 350 to 700 nm), rate of data acquisition: 10 μ s/sample to 1000 μ s/sample. A micro cuvette of 30.2 μ l volume is used. The equipment has < 3 ms dead time (depending on the flow rate used)³⁹. The Dynamic light scattering instrument from Brookhaven [Model BI-200SM] is used to estimate final particle size.

4.2 Reaction protocol

The reduction of gold chloride by tannic acid to form gold nanoparticles⁴⁰ is investigated in this study. The reagents are H₂AuCl₄ at pH 3.15 and tannic acid at a pH of 7.73. The expected stoichiometry is



The process was studied at two different temperatures, namely 25°C and 60°C. At each temperature, the concentration of gold chloride was varied (From 0.318 mM to 0.063 mM) keeping the molar ratio of tannic acid to gold chloride fixed at 2.08.

Chapter 5

Results

5.1 Performance characterization of SFM

To verify the mixing performance of SFM and to find its range, we studied the mixing of DCIP (Dichlorophenolindophenol) with water and followed the changes in absorbance. Figure 5.1 shows the spectra of DCIP obtained using a standard UV-Vis spectrometer (Shimadzu, model UV-2101).

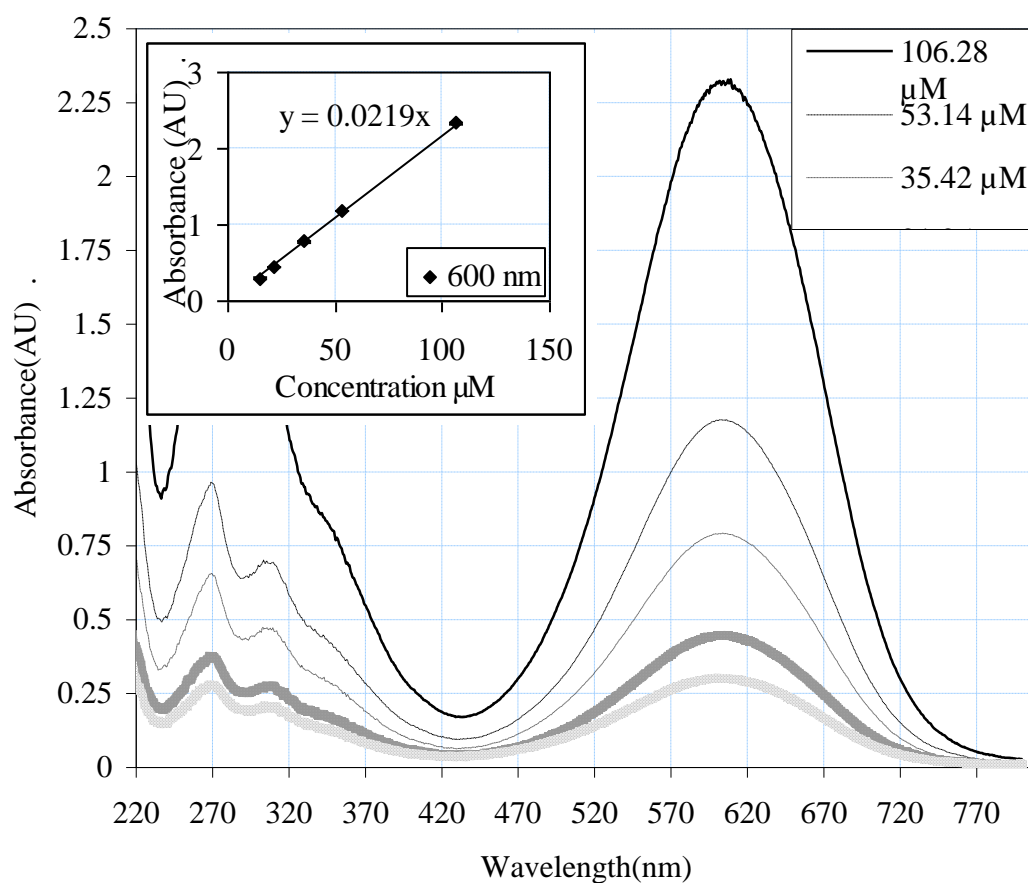


Figure 5.1: Absorbance spectrum of Dichlorophenolindophenol (DCIP) at different concentrations, obtained using a Shimadzu UV-Vis spectrophotometer inset shows the calibration curve

The inset shows that the variation of the absorbance at 600 nm with DCIP concentration has a slope of $0.0219 \mu\text{M}^{-1} \text{cm}^{-1}$. This value is almost similar to the

expected molar excitation coefficient of DCIP at 60 nm of $0.022 \mu\text{M}^{-1} \text{cm}^{-1}$ ⁴². These results show that DCIP is an appropriate test system for probing the capabilities of SFM.

These test results show that DCIP is an appropriate test system for probing the capabilities of SFM.

The SFM has two lamps, the Xe(Hg) lamp has higher intensity, however it is not feasible with the current SFM hardware to accurately subtract the intense peaks of Hg from the measured spectra. The Figure 5.2 is the absorbance spectrum obtained for different concentrations of DCIP in SFM.

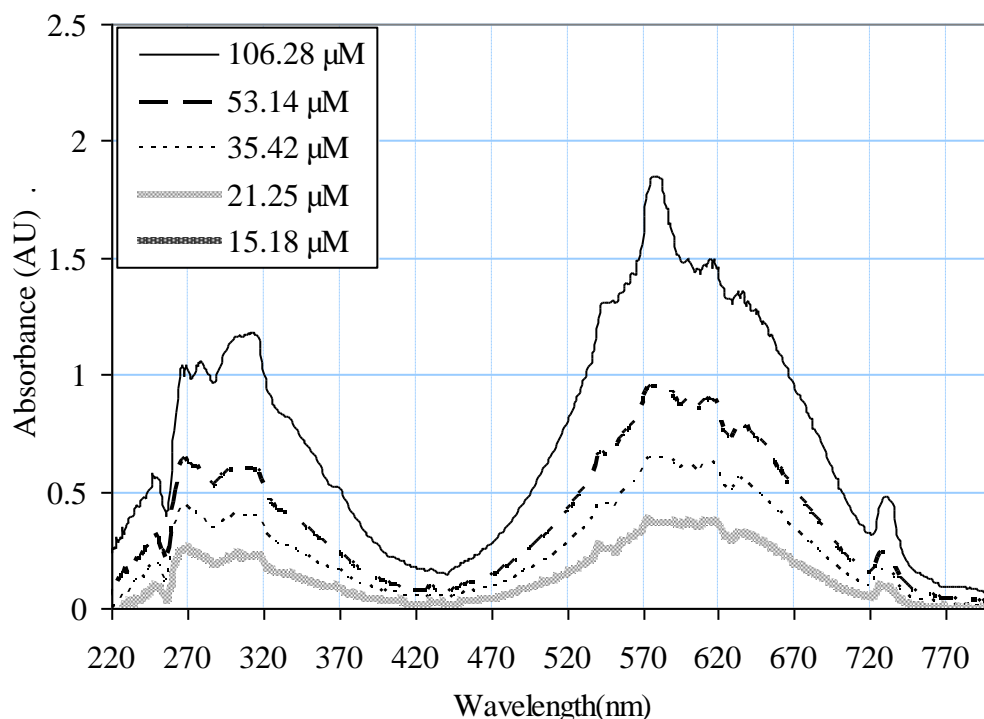


Figure 5.2: Absorbance spectrum of Dichlorophenolindophenol obtained from SFM showing the presence of features attributed to (Xe(Hg)) lamp peaks

So, the Xe lamp was used and figure 5.3 highlights the limitations of using a Xe lamp. The saturation of 600 nm peak of DCIP spectrum at an absorbance of 1.5 indicates a limitation on the maximum absorbance that can be measured. Also it can be seen that , 350 nm, the signal is poor leading to lower measured absorbance. The lower limit on absorbance is set by the background noise level and is 0.05 (AU) with the Xe lamp.

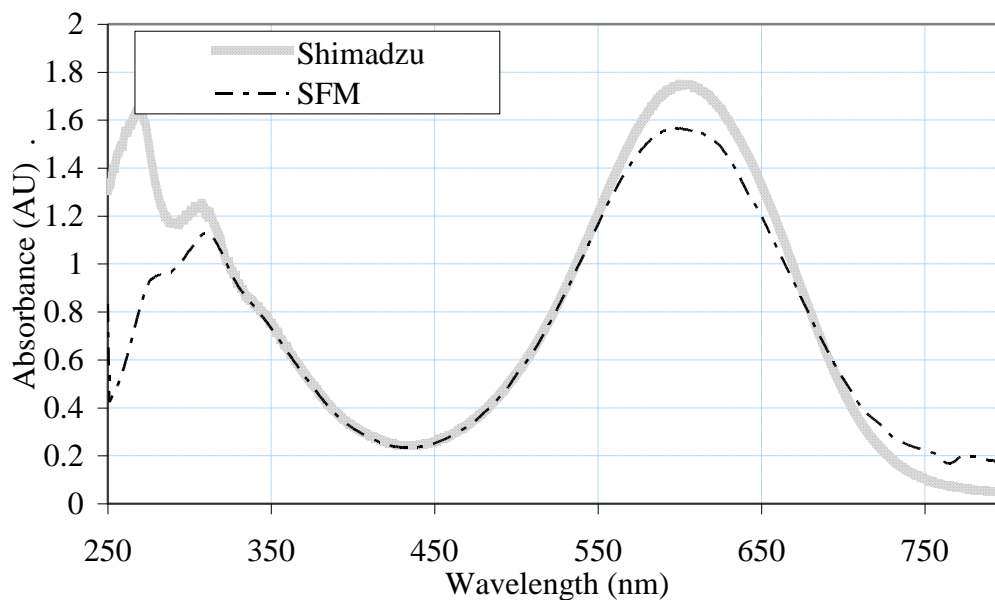


Figure 5.3: The spectrum of DCIP obtained from Simadzu spectrometer and SFM. The absorbance of SFM is getting saturated at 1.5 AU. hence its the upperlimit of absorbance that can be obtained from SFM.

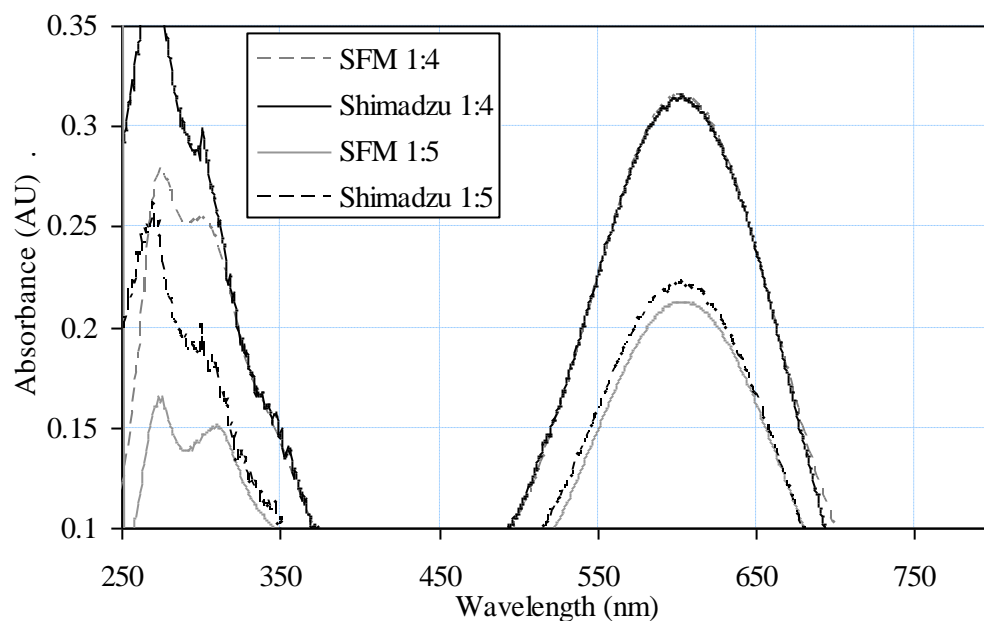


Figure 5.4: DCIP absorbance spectrum obtained from SFM vs. Shimadzu spectrometer, 1:4 mixing ratio of 1(DCIP in syringe S4): 4(water in syringe S2) and mixing ratio of 1:5. The absorbance obtained from SFM starts deviating from expected absorbance.

The mixing efficiency of SFM was tested by diluting DCIP with water in volumetric ratios ranging from 1:1 to 1:5. Figure 5.4 shows a comparison of the absorbance at 600 nm that is expected (Based on the concentration obtained using a standard Shimadzu spectrometer) and that measured in SFM. It is clearly seen that for volumetric ratios higher than 1:4, the absorbance measured using SFM deviates significantly from the expected value. Hence all the further experiments were conducted within these limits of SFM.

5.2 Optimizing protocol for studying gold nanoparticle formation

An initial experiment was conducted using Global mode. This mode allows the kinetics at different wavelengths to be collected in a serial manner, automatically. However, it does not allow intermittent washing. Also, it requires longer durations (5 hours). To verify the stability of tannic acid at the reaction conditions (ie. pH of 7.73), its UV-Vis spectra was monitored over 6 hrs.

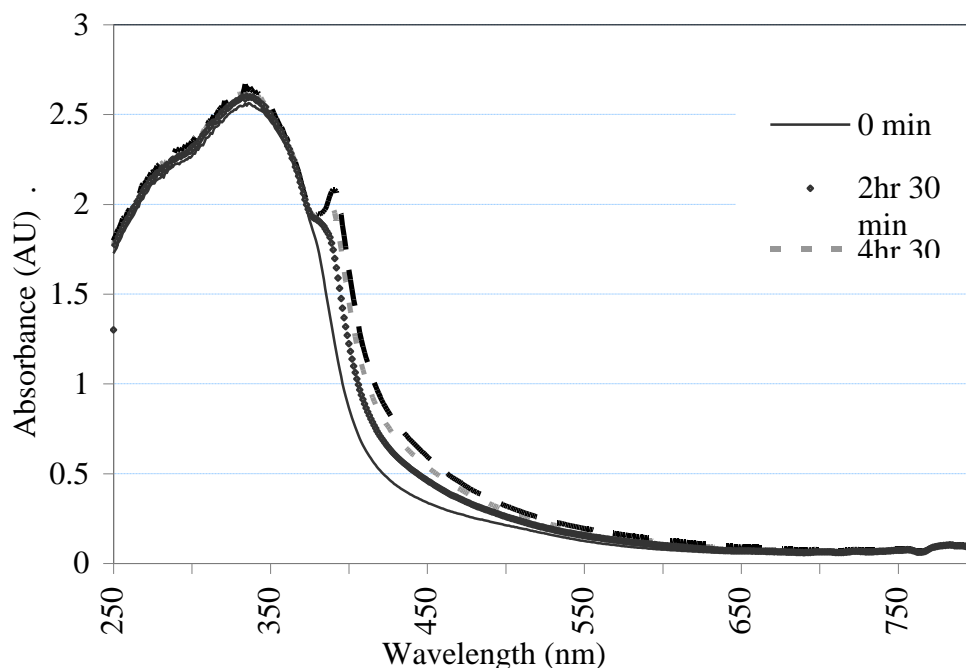


Figure 5.5: Tannic acid degradation at a pH 7, monitored by changes in absorbance curve in SFM at different time intervals, the shoulder at 390 nm increases with time showing some changes occur with increase in time. The shoulder started appearing at 2.30 hrs.

Figure 5.5 shows the spectra of tannic acid at pH 7.73 ageing. It is seen that after 2.5 hours the spectra of tannic acid changes with an additional peak at 420 nm. This sets an upper-limit for duration of global mode experiments.

Figure 5.6 is a plot of data obtained using global mode analysis. It is seen that the higher wavelengths the measured absorbance is large even in the initial periods. This is attributed to the deposition of gold nanoparticles formed in the earlier runs (i.e. when kinetics at smaller wavelengths were captured). This implies that global mode is not a viable option for nanoparticle systems and also that a viable cleaning protocol needs to be evolved for obtaining consistent and repeatable results with SFM.

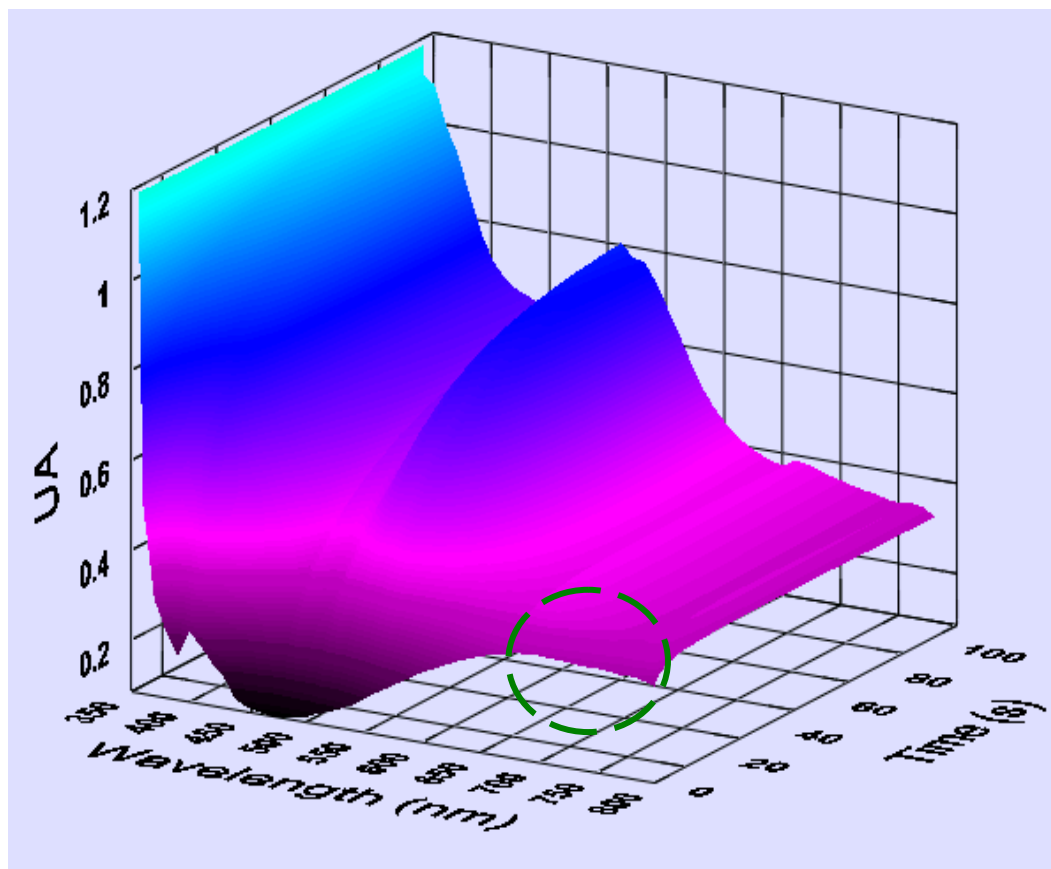


Figure 5.6: A screenshot of the global mode in SFM, obtained for preparation of gold nanoparticles. Global mode (3D analysis) gives temporal evolution of the spectra. The nanoparticle peak was present at 530 nm. The circle shows the high absorbance's even at $t=0$ for wavelengths > 550 nm.

The optimized protocol consists of the following steps:

- 10 ml of concentrated aqua-regia was prepared,
- This was made to 40 ml using DI water
- Each 10 ml syringe was filled and 1ml was flushed from each syringe (to fill the flow lines and cuvette with dilute acid)
- After 10 min, the system was flushed with 80 ml of DI water. (20 ml water from each syringe)
- 1 ml of 1% w/v K_2CO_3 was made to 40 ml using DI water and was flushed through the system.
- Further 120 ml of DI water was flushed through the system (30 ml from each syringe)

The pH of the final wash water was checked to make sure washing was proper. The flow rate during all the washing processes was 0.5 ml/s.

5.3 Kinetics of gold nanoparticle formation

The kinetics of gold nanoparticle formation were observed by measuring the absorbance changes at 530 nm and 522 nm for experiments conducted at 25°C (figure 5.7) and 60 °C (figure 5.8) respectively. At each temperature, five different concentrations of $HAuCl_4$ were used (At a fixed molar ratio of tannic acid to gold chloride) and each experiment was repeated thrice and reproducibility of the result was ensured. In all experiments, contribution of excess tannic acid had been removed before further analysis.

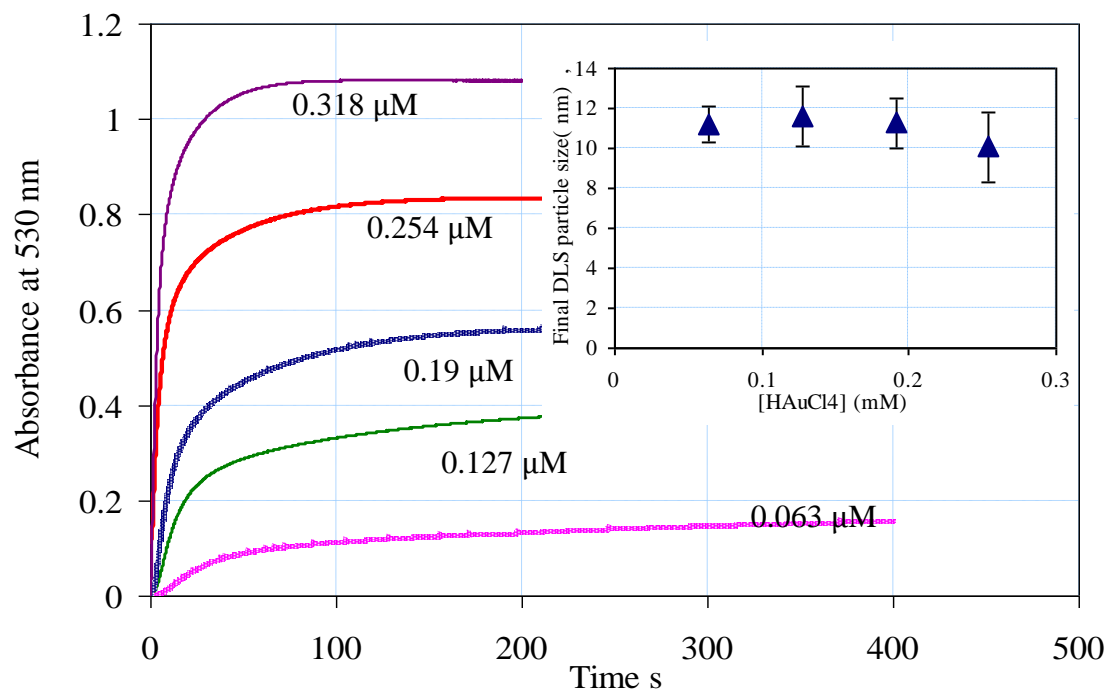


Figure 5.7: Average absorbance vs. t plots, obtained for different concentrations gold salt with constant molar ratio tannic acid to gold at 25°C. The final absorbencies scale according to the concentration of gold salt used.

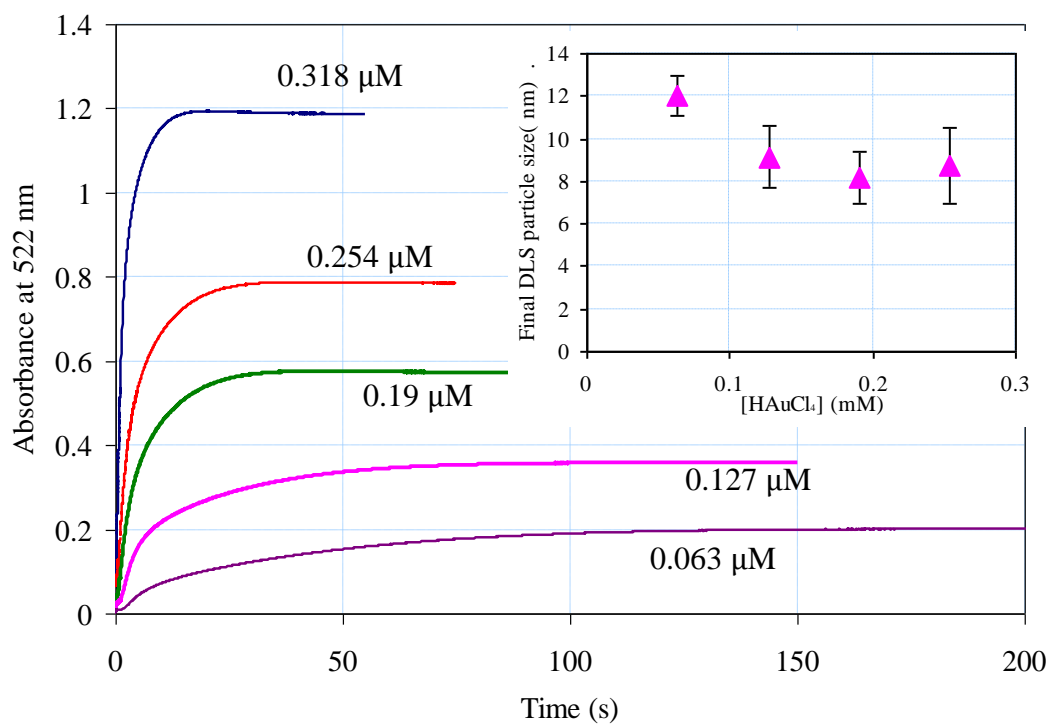


Figure 5.8: Average absorbance vs. t plots, obtained for different concentrations gold salt with constant molar ratio tannic acid to gold at 65°C. The final absorbencies scale according to the concentration of gold salt used.

The absorbance curve typically show a sigmoidal nature associated with autocatalytic reactions. The induction time and initial slopes were analyzed and the results are presented in the following sections. Another interesting aspect is that the final absorbance values scale linearly with initial concentration of HAuCl_4 .

Table 5.1: Average particle diameters obtained for different initial concentrations of gold chloride

[HAuCl_4] mM	Average particle size at 25 °C \pm SD	Average particle size at 60 °C \pm SD
0.2544	10.06 \pm 1.8	8.75 \pm 1.5
0.1908	11.29 \pm 1.2	8.182 \pm 2.3
0.1272	11.62 \pm 1.5	9.155 \pm 1
0.0636	11.22 \pm 1	12.001 \pm 4.2

Figure 5.7 and 5.8 inset, shows the plot of final hydrodynamic particle size (Table 5.1) for 2 ml of the samples collected after mixing in SFR at the two different temperatures. It is seen that only the number of particles produced varies linearly with initial HAuCl_4 concentration.

Neglecting coagulation, these results imply that the number of nuclei formed varies linearly with initial HAuCl_4 concentration. Assuming that all nucleation occurs within the induction period, a plot of nucleation rate vs. initial HAuCl_4 concentration will be as shown in figure 5.9. Table 5.2 presents the average nucleation rate as a function of varying concentration.

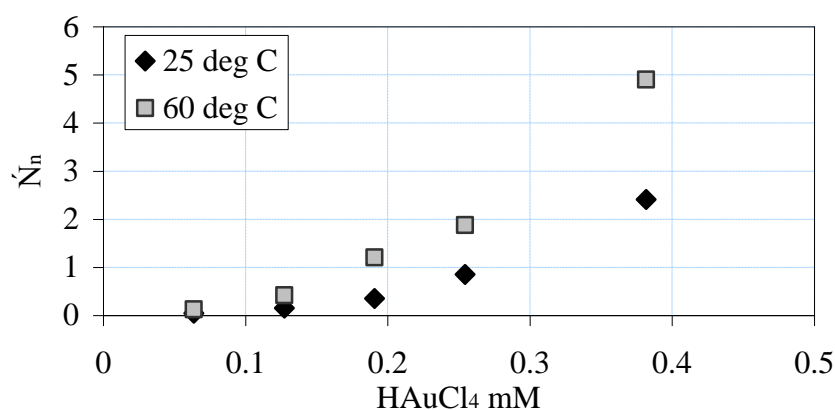


Figure 5.9: Nucleation rate as a function of varying concentration and temperature

Table 5.2: Variation of induction time, particles per cuvette volume and nucleation rate at different temperatures and concentrations

[HAuCl ₄]	Temperature °C	$t_{ind} \pm$ Standard deviation	No. of particles/ (30.2 μ l cuvette) *10 ⁹	Nucleation rate (particles/sec)*10 ¹⁰
0.00038	25	0.61 \pm 0.07	9.805	2.41
0.00025	25	1.15 \pm 0.17	8.55	0.8526
0.00019	25	2.07 \pm 0.25	6.41	0.355
0.00013	25	3.27 \pm 0.48	4.275	0.15
6.4E-05	25	5.16 \pm 0.34	2.14	0.0475
0.00038	60	0.3 \pm 0.06	9.805	4.9
0.00025	60	0.52 \pm 0.06	8.55	1.88
0.00019	60	0.61 \pm 0.03	6.41	1.205
0.00013	60	1.16 \pm 0.05	4.275	0.42
6.4E-05	60	1.91 \pm 0.63	2.14	0.128

Note: an average diameter of 8 nm is assumed (based on a TEM image)

5.4 Induction time

As seen in chapter 2, the variation of induction time with supersaturation on reagent concentration can be analyzed using the kinetic theory of nucleation or classical nucleation theory. The solubility of gold in aqueous solution is assumed to be 2×10^{-12} mol/l (approximate value obtained from reference 34, for silver) for these computations. Figure 5.10 shows induction time vs. initial gold chloride concentration plotted according to the relationship expected according to the kinetic theory of nucleation at two different temperatures and slopes are found to be ~ 1 . Which implies that the number of monomers in critical nuclei is ~ 2 . This result is in concord with analysis of induction time in similar precipitation processes⁴³ and can be justified based on the account of very low solubilities of monomer.

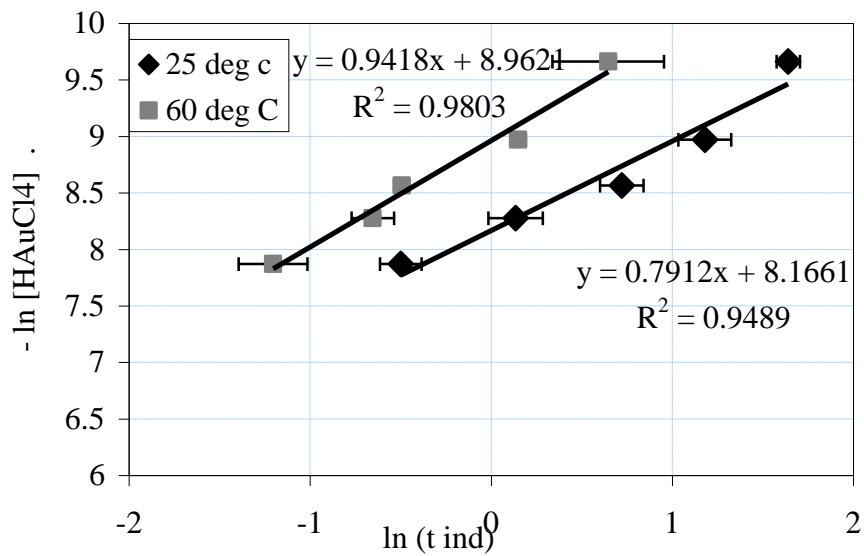


Figure 5.10: Variation of induction time as a function of initial goldchloride concentration as per kinetic theory

The experimental induction times are plotted in fig 5.11 as per the classical nucleation theory and hence also the data show a linear relationship.

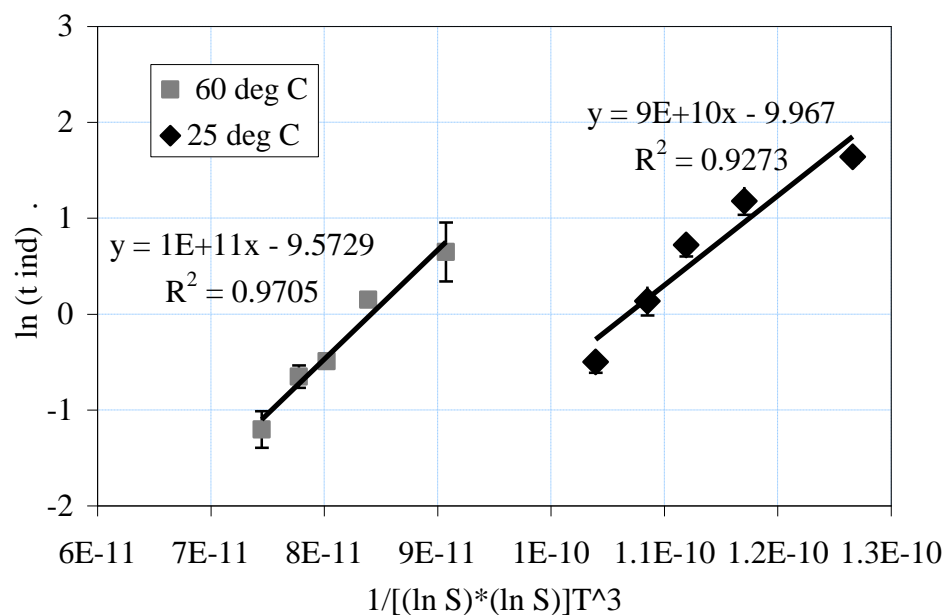


Figure 5.11: Variation of induction time as a function of supersaturation based on classical nucleation theory

However, the value of surface energy extracted from the slope (assuming $V_m = M/(\rho N_A)$) is $1.939 \times 10^{-5} \text{ mJ/m}^2$, which is several orders of magnitude different from experimentally determined value of 580 mJ/m^2 reported in literature³⁴.

The analysis of induction time according to classical nucleation theory and kinetic theory assume all the monomer has been formed prior to nucleation and that the time taken for reaction is negligible. This assumption is not valid for typical precipitations and so, more detailed models are needed to understand the kinetics of induction time. However these initial attempts provide a starting point for more refined analysis.

5.5 Growth kinetics

As seen earlier, surface reaction controlled growth mechanisms or bulk reaction rate (supply) limited growth are two plausible mechanisms for modelling nanoparticle growth. Considering the autocatalytic nature of these growth mechanisms and the small masses involved in nucleation, diffusion can be safely ignored in this regime. If polynuclear or mononuclear growth processes are the rate limiting steps, then one would expect the volume of nanoparticles to vary as

$$\frac{1}{V^{2/3}} \frac{dV}{dt} = k \left(V_m (C_b - C_e) \right), \text{ for surface deposition controlled (polynuclear) process} \quad (5.1)$$

$$\frac{1}{V^{2/3}} \frac{dV}{dt} = k V^{2/3} \left(V_m (C_b - C_e) \right), \text{ for surface deposition controlled (mononuclear) process} \quad (5.2)$$

respectively.

Given that the absorbance \propto volume (for $< 20 \text{ nm}$) and the initial growth period (i.e. $C_b \sim \text{constant}$) these equations imply that

$$A^{1/3} = Bt + C \text{ for polynuclear surface deposition controlled growth,} \quad (5.3)$$

$$\text{And, } A^{-1/3} = Dt + E \text{ for mononuclear surface deposition controlled growth.} \quad (5.4)$$

Figure 5.12 shows the data at various concentrations fitted to either of these equations.

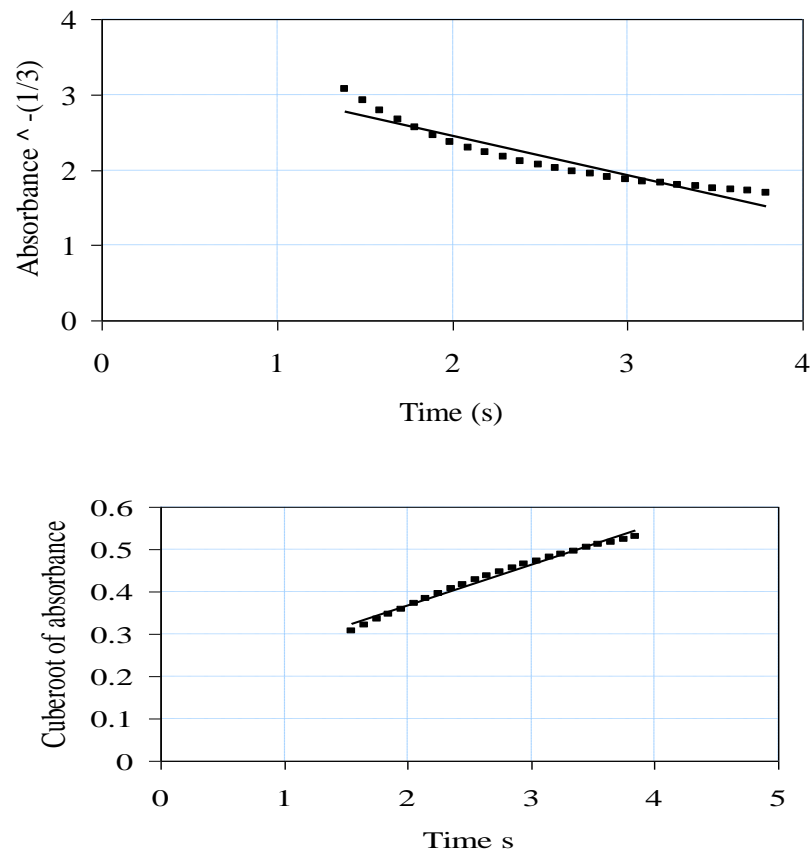


Figure 5.12 Initial slopes fits for polynuclear and mononuclear growth models

It is clearly seen that only polynuclear growth model fits the experimental data over initial growth period. The values of initial slopes for various experimental conditions are tabulated in table 5.3.

Now B (slope determined from experiment) = $C_{Aub} \Big|_{t=t_{ind}} * K_{surface \text{ reaction}}$ (Assuming first order surface reaction)

Where, $K_{surface \text{ reaction}}$ is rate of growth. Assuming that $C_{Aub} \Big|_{t=t_{ind}} \sim C_{HAuCl_4} \Big|_{t=t_{ind}}$ one would expect a plot of B vs $C_{HAuCl_4} \Big|_{t=t_{ind}}$ linear with intercept at origin. Figure 5.13 shows this to be the case and so it could be concluded that the polynuclear surface reaction is indeed the growth mechanism followed initially.

Table 5.3: Values of best fit initial slopes obtained for different temperatures and concentrations

S. No.	HAuCl ₄ (mM)	Temperature °C	Value of best-fit initial slope
1	0.3816	25	0.23
2	0.2544	25	0.12
3	0.1908	25	0.06
4	0.1272	25	0.03
5	0.0636	25	0.01
6	0.3816	60	0.43
7	0.2544	60	0.25
8	0.1908	60	0.25
9	0.1272	60	0.1
10	0.0636	60	0.05

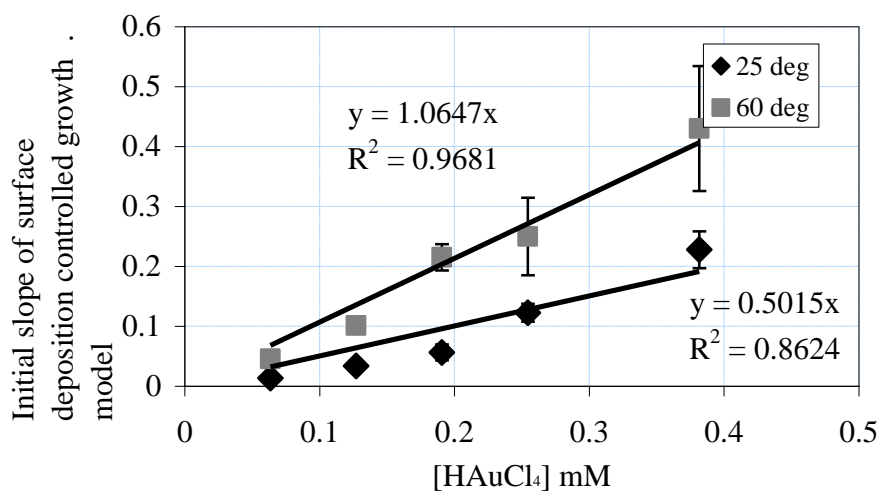


Figure 5.13: Plot showing linear dependence of initial slope values obtained from the surface deposition controlled growth ($A^{1/3}$ vs. t graph) with respect to $[HAuCl_4]$ concentration ratios

At longer times absorbance grows more slowly than expected by surface reaction, which implies that bulk reaction rate controls the growth rate. Assuming that the bulk reaction follows the following power law trend with rate constant k' ;

$$\frac{d[\text{Au}^0]}{dt} = k'[\text{HAuCl}_4]^n \quad (5.5)$$

Tannic acid is in excess, hence its effect is not considered. The data were analyzed using the half life method⁴⁴ to find the best fit value of n. this analysis implies that

$$t_{1/2} = \frac{(0.5)^{1-n} - 1}{k'(n-1)} [\text{HAuCl}_4]^{1-n} \quad (5.6)$$

where, $t_{1/2}$ is the time required for half of the initial reactant to be consumed. And these $t_{1/2}$ values are tabulated in table 5.4 and plotted according to equation 5.6 by taking log on both sides. From the plot it is seen that the reaction order is ~ 2.3 under these experimental conditions.

Table 5.4: Half life times for different temperatures and concentrations

S. No.	[HAuCl ₄]	Temperature °C	$t_{1/2}$ (s)
1	0.3816	25	3.65
2	0.2544	25	7.66
3	0.1908	25	13.53
4	0.1272	25	22.02
5	0.0636	25	36.67
6	0.3816	60	1.8
7	0.2544	60	3.55
8	0.1908	60	3.97
9	0.1272	60	7.83
10	0.0636	60	21.21

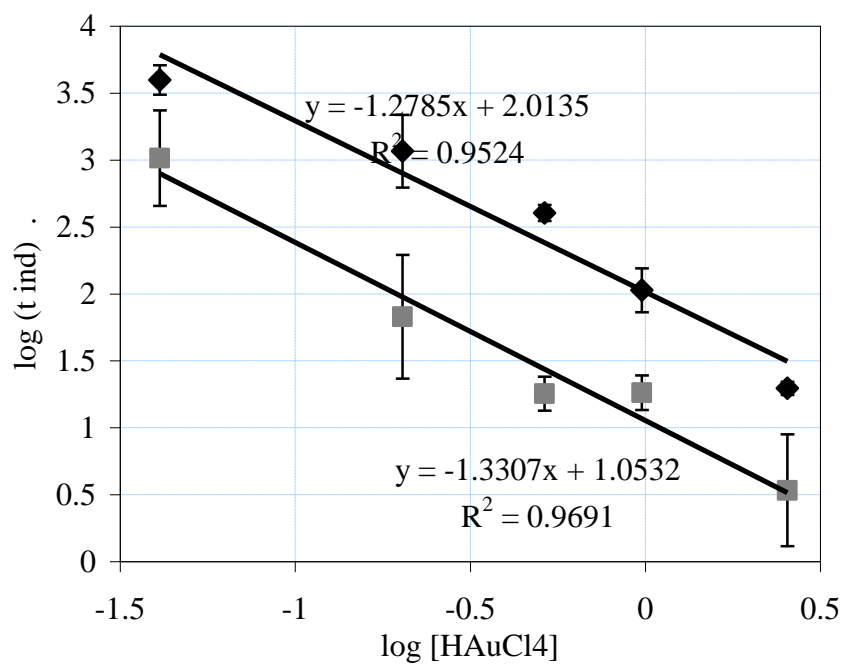


Figure 5.14: The plot of gold chloride concentration vs. half life period, plotted for reactions at 2 different temperatures. This gives us an approximate estimate of reaction order

Chapter 6

Conclusions

The conclusions based on the results and analysis of the data presented earlier are summarized below

- The optimum protocol for studying gold nanoparticle formation has been established.
- Preliminary analysis indicates that critical nuclei size is very small (~ 2 atoms) and that the growth is dominated by polynuclear surface reaction initially and then latter on by bulk reaction rate.
- The order of bulk reaction rate is found to be ~ 2.3 with respect to HAuCl_4 .

Further, these data and the fact that final particle size is almost independent of initial HAuCl_4 concentration will be useful in discriminating between more detailed models to be developed in the future.

Chapter 7

References

1. www.nanocompositech.com/glossary-nanocomposit-nanotechnology.htm., accessed on 10/ 01/ 2007.
2. Schmidt, G. Nanoparticles- From Theory to Application. Wiley-VCH Verlag Gmbh and Co., **2004**.
3. Halperin, W. P. (1986). Quantum size effects in metal particles. *Rev. Mod. Phys.* , **1986**, 58, 3.
4. Gu, N.; Huang, L.; Xu, L. N.; Liao, J. H.; Zhang, Y.; and Wang, M. Study of Fabricating Functional Nanostructure through combined with Molecular Assembly. *IEEE* , **2003**, 806.
5. Mayhew, M. T.; Griffiths, G.; and Lucocq, M. J. Applications of an efficient method for comparing immunogold labeling patterns in the same sets of compartments in different groups of cells. *Histochem. Cell. Biol.* , **2004**, 122, 171.
6. www.devicelink.com/ivdt/archive/00/03/004.html., accessed on 10/ 01/ 2007.
7. Slot, W. J.; and Geuze, J. H. A new method of preparing gold probes for multiple-labeling cytochemistry. *Eur.J. Cell Biol.*,**1985**, 38, 87.
8. Mantzaris, V. N. Liquid-phase synthesis of nanoparticles: Particle size distribution dynamics and control. *Chem. Eng. Sci.*, **2005**, 4749.
9. Kimling, J.; Maier, M.; Okenve, B.; Kotaidis, V.; and Ba, H. Turkevich Method for Gold Nanoparticle Synthesis Revisited. *J. Phys. Chem. B* , **2006**, 110, 15700.
10. Turkevich, J.; Stevenson, P. C.; and Hiller, J. A study of the nucleation and growth processes in the synthesis of colloidal gold. *J. Discuss. Faraday Soc.* , **1951**, 11, 55.
11. Wang, W.; and Li, Y. ‘Monodisperse nanocrystals: general synthesis, assembly, and their applications. *Chem. Commun.* , **2007**, 2901.

12. Brust, M.; Walker, M.; Bethell, D.; and Schiffrin, J. D. Synthesis of thiol-derivatised Gold Nanoparticles in a two phase liquid-liquid System. *J. Chem. Soc. Commun* , **1994**, 801.
13. Herrera, P. A.; Resto, O.; Briano, G. J.; and Rinadi, C. Synthesis and agglomeration of gold nanoparticles in reverse micelles. *Nanotechnology* , **2005**, 16, S618.
14. Chance, B. The stopped-flow method and chemical intermediates in enzyme reactions-a personal essay. *Photosynth. Res* , **2004**, 80, 387.
15. Kresge, N.; Simoni, R. D.; and Hill, R. L.; B. Chance: Olympian and developer of stop-flow methods. *J. Biol. Chem.*, **2004**, 279, 109.
16. www.bio-logic.info/rapid-kinetics/index.html (accessed on 08/ 20/ 07).
17. LaMer, V. K.; and Dinegar, R. H. Theory, production and mechanism of formation of monodispersed hydrosols. *J. Am. Chem. Soc.* , **1950**, 72, 4847.
18. Nancollas, G. H.; and Purdie, N. The kinetics of nucleation. *Quart. Rev. (London)* , **1964**, 18, 1.
19. Nyvlt, J.; Sohnel, O.; Matuchova, M.; and Broul, M. The kinetics of industrial crystallization. Elsevier science publishers, **1985**.
20. Sugimoto, T. Monodispersed Particles. Elsevier: Amsterdam, **2001**.
21. Kelly, K. L.; Coronado, E.; and Zhao, L. L. The optical properties of metal nanoparticles: The influence of size, shape, and dielectric environment. *J. Phys. Chem B*, **2003**, 107, 668.
22. Abescassis, B.; Testard, F.; Spalla, O.; and Barbo, P. Probing insitu the nucleation and growth of gold nanoparticles by small-angle X-ray scattering. ', *Nano letters.*, **2007**, 7, 1723.
23. Link, S.; and El-Sayed, M. A. Shape and Size dependence of radiative, non-radiative and photothermal properties of gold nanocrystals. *Int. Rev. Phys. Chem* , **2000**, 19, 3, 409.
24. Roelands, C. P.; Horst, C.; Kramer, H. J.; and Jansens, P. J. Analysis of Nucleation Rate Measurements in Precipitation processes. *Cryst. Growth Des.*, **2006**, 6, 1380.

25. Berger, R. L.; Balko, B.; and Chapman, H. F. High resolution mixer for the study of the kinetics of rapid reactions in solution. *Rev. Sci. Instr.* **1986**, 39, 486.
26. Wang, X.; ZHuang, J.; Peng, Q.; and Li, Y. A general strategy for nanocrystal synthesis. *Nature* , **2005**, 437, 121.
27. Bao, Y.; Pakhomov, A. B.; and Krishnan, K. M. A general approach to synthesis of nanoparticles with controlled. *J. App.Phy.*, **2005**, 97, 10J317.
28. www.patentstorm.us/patents/7160525.html., accessed on 09/ 20/ 07.
29. Daniel, M. C.; and Astruc, D. Gold Nanoparticles: Assembly, Supramolecular Chemistry, Quantum-Size-Related Properties, and Applications toward Biology, Catalysis, and Nanotechnology. *Chem. Rev.* , **2004**, 104, 293.
30. Cushing, L. B.; Kolesnicheko, L. V.; and O'connor, J. C. Recent advances in the liquid-phase synthesis of inorganic nanoparticles. *Chem. Rev.* , **2004**, 104, 3893.
31. Mulphordt, H. 'The preparation of colloidal gold particles using tannic acid as the additional reducing agent. *Experientia* , **1982**, 38.
32. Jana, R. N.; and Peng, X. Single-phase and Gram-scale routes toward nearly monodisperse Au and other noble metal nanocrystals. *J. Am. Chem. Soc.* , **2003**, 125, 14280.
33. Arcoleo, V.; and Liveri, V. T. AFM investigation of gold nanoparticles synthesized in water/AOT/n-heptane microemulsions. *Chem. Phys. Lett.*, **1996**, 258, 223.
34. Ghader, S.; Manteghian, M.; Kokabi, M.; & Mamoory, R. S. Induction time of reaction crystallization of silver nanoparticles. *Chem. Eng. Technol.* , **2007**, 30, 1129.
35. Andreescu, D.; Sau, T. K.; and Goia, D. V.; Stabilizer free nanosized gold sols. *J. Colloid. Interface Sci.*, **2006**, 298, 742.
36. Salvati, R.; Longo, A.; Carotenuto, G.; and Nicola, S. D. O-line monitoring of Au nanoparticles formation by optical spectrophotometry. *Eur. Phys. J.* **2004** , B 41, 43.
37. Pong, B. K.; Elim, I. H.; Chong, J. X.; Ji, W.; Trout, L. B.; and Lee, J. X. New insights on the Nanoparticle growth mechanism in the citrate reduction of

- gold(III) salt: Formation of the Au Nanowire intermediate and its Nonlinear optical properties. *J. Phys. Chem. C* , **2007**, 111, 6281.
38. Salvati, R.; Longo, A.; Carotenuto, G.; De Nicola, S.; Pepe, G.P.; Nicolais, L.; and Barone, A. UV-vis spectroscopy for on-line monitoring of Au nanoparticles size during growth. *Appl. Sur. Sci.*, **2005**, 248, 28.
39. SFM-300/400 User's Manual, ver.2.3. **2006**.
40. Kalidas, S.S.; and Santhanam, V. unpublished manuscript
41. Chakraborty, J. Modelling of synthesis of nanoparticles and development of techniques for simulation. Phd. Thesis, **2008**, IISc.
42. Finn, R. D.; Basran, J.; Roitel, O.; Wolf, C. R.; Munro, A. W.; Paine, M. J. I.; and Scrutton, N. S. Determination of the redox potentials and electron transfer properties of the FAD- and FMN-binding domains of the human oxidoreductase NR1. *Eur. J. Biochem* , **2003**, 270, 1164.
43. Burgues, J. T. Test of nucleation models from compiled data. *Port. Electrochim. Acta*, **2007**, 25, 273.
44. Levenspiel, O., Chemical reaction engineering, Wiley: Singapore, **2004**

Appendix I: SFM operation procedure

Procedure during start up:

1. Start the software by clicking the Biokine icon in the desktop.
2. Click “Install” → “Device installation” → “Select MOS – 200/M” → “Use stopped flow” (check) → Serial port Com 1 → “OK”
3. “Install” → “Stopped flow configuration” you will get a pop up window.
4. select “-400/S”, “Stopped flow advanced mode”, and “10 ml/ 20 mm/ 4mm for -300&400(std) for all syringes., click “OK”

MOS-200/M calibration:

1. Click “Install” → “Device installation” (pop up window) → “Select MOS-200/M” → “Use stopped flow”(check) → Serial port “com1” → “ok”
2. “Device” → Scanning Spectrometer, (Spectrometer window is loaded)
3. Click “Acquisition setup” (pop up window “ Scanning setup” will appear)
4. Select “Absorbance” in Acquisition mode.
5. Set scan parameters: (note: we want to observe 546nm of Xe(Hg) spectrum)

Begin: (eg.500 nm)

End: (eg. 600 nm)

Scan repeat: 1

Acquisition duration(s): .05

click “ok”
6. Click “HV on” and “Auto”, the voltage will vary, wait until a stable value appears and click “Auto” again

7. Record reference spectrum.
8. A clear peak at 546 nm must be noted else set the monochromator at maximum peak intensity, close the window
9. click “Install” → “Spectrometer advanced settings” → Click “Calibration” opens pop up window
10. enter 546 in text box → “ok”
11. Repeat steps 1 to 6, a peak must be observed at 546 nm.
12. Click “Initialization” (Monochromator gets initialized)

Checking lamp alignment:

1. In Main menu, “Install” → “Stopped flow configuration” → “Device” → “400/S” → “OK”
2. MOS-200/M (Hardware setup) →
 - a. “Excitation wavelength” (beg. 524) → “Apply” → “Exit”

Note: the wavelength of interest must be applied
3. “Device” → “transient recorder” → Excitation in progress → appearance of graphical screen with Volt (V) Vs Time (s).
4. Acquisition setup:

Set 1: Mode-Fluorescence/ Volts; Set 2: Mode - None


Time base: 1

Number of points (max.) = 8000.

No Trigger
5. HV on → “Auto” → Click “Auto” again when a stable value is reached. (Its usually around 300v for 524nm wavelength)
6. Align the lamp so as to obtain a maximum and stabilized voltage signal in the range 0-10 V(it should be preferably greater than or equal to 5 V)

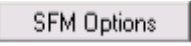
Controlling and initializing syringes:



1. Click “” button in the stopped flow status area “Syringe command” pop up window will appear.
2. Bring all syringes to up position using the “up” button in MPS unit.

3. Click “reset all”——→all syringes are reset
4. Adjust manual speed to 4 ml/s (advised for 10 ml syringes in manual)
5. Attach a syringe (disposable plastic syringes may be used) containing sample or buffer to a syringe reservoir port on top of the SFM
6. Set the syringe valve handle to (**R**) and fill the syringe manually, while exerting a slight pressure on the reservoir syringe
7. Eliminate any bubbles in the SFM syringe by driving the SFM syringe up and down several times while it is connected to the reservoir syringe
8. Turn the syringe valve handle to (**C**)
9. Empty one or two elementary movements of the syringe, till you observe liquid flowing out. (to definitively eliminate any bubbles remaining in SFM and cuvette)
10. Repeat the above process for the other syringes.
11. It is recommended that the syringes be filled in reverse numerical order to best remove bubbles from the SFM and cuvette.

Stopped flow sequence/ mixing sequence:

1. Click “Mixing sequence” button in the stopped flow status area. Pop up window will appear
2. First operation should be to check the configuration of the stopped-flow, it is made by clicking on the  button.
3. Select the **cuvette** and **mixer** according to the cuvette and mixer installed in the SFM (don't check HDS mixer), valve lead=0
4. Set mixing ratio according to concentration required
5. Adjust the total volume by up or down arrows. The volume from each syringe is automatically calculated. Adjust according to color codes
6. Total flow rate must be selected using ‘up’ and ‘down’ arrows. Once the total flow rate selected the flow rate for each syringe is automatically calculated. Adjust according to color codes
7. click “At stop”
8. Enter syringe contents and concentrations. The final concentrations are automatically calculated.

9. Click “Ready”
10. In stopped flow menu bar, “shot control window” will appear. (number of possible shots is visible there)

Spectral analysis:

1. Click “Install” → “Device installation” (pop up window) → “SelectMOS-200/M → “Use stopped flow” (check) → Serial port “com1” → “ok”
2. Check if valve is in “C” position else set it to “C” position.
3. Click Mos200/M → Excitation → Set wavelength of excitation as “ the maximum lamp peak in the required range”
4. “Device” → Scanning Spectrometer, (Spectrometer window is loaded)
5. Click “Acquisition setup” (pop up window “ Scanning setup” will appear)
6. Select “Absorbance” in Acquisition mode.
7. Set scan parameters: (note: a, b depending on desired wavelength)

Begin: (eg. a nm)

End: (eg. b nm)

Scan repeat: 1

Acquisition duration(s):

click “ok”

8. click “HV on” and “ Auto”, wait till voltage stabilizes and click “ Auto” again
9. Record reference spectrum
10. Click “record” under Blank spectrum
11. save the spectrum obtained
12. Now send 3 or 4 shots such that the volume of mixture is thrice the dead



volume from last mixer. (click arrow button in “

13. Now click the “Arrow” under Acquisition to get the spectrum